Solid State Ionics 344 (2020) 115155

Contents lists available at ScienceDirect

Solid State Ionics

journal homepage: www.elsevier.com/locate/ssi

Oxygen transport in Pr nickelates: Elucidation of atomic-scale features

Vladislav Sadykov[a,b,*], Elena Pikalova[c,d], Nikita Eremeev[a], Aleksandr Shubin[a,b], Igor Zilberberg[a,b], Igor Prosvirin[a,b], Ekaterina Sadovskaya[a,b], Andrey Bukhtiyarov[a]

[a] Federal Research Center Boreskov Institute of Catalysis, Lavrentiev Ave. 5, Novosibirsk 630090, Russia
[b] Novosibirsk State University, Pirogova st. 2, Novosibirsk 630090, Russia
[c] Institute of High Temperature Electrochemistry UB RAS, Akademicheskaya st. 20, Yekaterinburg 620137, Russia
[d] Ural Federal University, Mira st. 19, Yekaterinburg 620002, Russia

ARTICLE INFO

Keywords:
$Pr_{2-x}Ca_xNiO_4$
Oxygen diffusion
X-ray photoelectron spectroscopy
Density functional theory calculations

Classification codes:
A0340K
A3365F
A6170B
A6170T
A6630D
A7511M

ABSTRACT

$Pr_2NiO_{4+\delta}$ oxide with a layered Ruddlesden–Popper structure is a promising material for SOFC cathodes and oxygen separation membranes due to a high oxygen mobility provided by the cooperative mechanism of oxygen migration involving both interstitial oxygen species and apical oxygen of the NiO_6 octahedra. Doping by Ca improves thermodynamic stability and increases electronic conductivity of $Pr_{2-x}Ca_xNiO_{4+\delta}$, but decreases oxygen mobility due to decreasing the oxygen excess and appearing of 1–2 additional slow diffusion channels at $x \geq 0.4$, probably, due to hampering of cooperative mechanism of migration. However, atomic-scale features of these materials determining oxygen migration require further studies. In this work characteristics of oxygen diffusion in $Pr_{2-x}Ca_xNiO_{4+\delta}$ (x = 0–0.6) are compared with results of the surface analysis by X-ray photoelectron spectroscopy and modeling of the interstitial oxygen migration by the plane-wave density functional theory calculations. According to the X-ray photoelectron spectroscopy data, the surface is enriched by Pr for undoped sample and by Ca for doped ones. The O1s peak at ~531 eV corresponding to a weakly bound form of surface oxygen located at Pr cations disappears at ~500 °C. Migration of interstitial oxygen was modeled for a *I4/mmm* phase of $Pr_2NiO_{4+\delta}$. The interstitial oxygen anion repulses the apical one in the NiO_6 octahedra pushing it into the tetrahedral site between Pr cations. The calculated activation barrier of this migration is equal to 0.585 eV, which reasonably agrees with the experimental value of 0.83 eV obtained by the oxygen isotope exchange method. At the same time, for the model compound $Ca_2NiO_{4+\delta}$, obtained by isomorphic substitution of Pr by Ca in $Pr_2NiO_{4+\delta}$, calculations implied formation of the peroxide ion comprised of interstitial and lattice oxygen species not revealed in the case of incomplete substitution (up to $PrCaNiO_{4+\delta}$ composition).

Hence, calculations in the framework of the plane-wave density functional theory provide a realistic estimation of specificity of oxygen migration features in $Pr_2NiO_{4+\delta}$ doped by alkaline-earth metals.

1. Introduction

$Pr_2NiO_{4+\delta}$ oxide with a layered Ruddlesden–Popper (R-P) structure is a promising material for SOFC cathodes [1–8], electrodes for electrolysers and reversible cells [9,10] and oxygen separation membranes [11–14] due to a high oxygen mobility provided by the cooperative mechanism of oxygen migration involving both interstitial oxygen species and apical oxygen of the NiO_6 octahedra, as well as intermediate values of thermal expansion coefficients (TECs) and stability to carbonization [3,5,11,15–20]. Doping is usually applied to diminish $Pr_2NiO_{4+\delta}$ phase instability in the temperature range of 850–1000 °C [21]. Particularly, it was found that doping by Ca improves thermodynamic stability of $Pr_2NiO_{4+\delta}$ at these temperatures, increases electronic conductivity, decreases the thermal expansion coefficient value and chemical interaction with a number of solid state electrolytes [6,20,22]. However, Ca-doping decreases oxygen mobility due to decreasing the oxygen excess and appearing of 1–2 additional slow diffusion channels at $x \geq 0.4$, probably, due to hampering the cooperative mechanism of oxygen migration [19,20,23,24]. However, atomic-scale features of Ca-substituted material determining oxygen migration require further studies.

Oxygen transport mechanism in first homologues of R-P phases was modeled by such methods as molecular dynamics (MD) [25–32] and density functional theory (DFT) calculations [23,30,32–40]. The dominating mechanism of oxygen transport in K_2NiF_4-like compounds is so-called *cooperative mechanism* (being also referred to as interstitialcy

* Corresponding author at: Federal Research Center Boreskov Institute of Catalysis, Lavrentiev Ave. 5, Novosibirsk 630090, Russia.
E-mail address: sadykov@catalysis.ru (V. Sadykov).

https://doi.org/10.1016/j.ssi.2019.115155
Received 21 July 2019; Received in revised form 11 November 2019; Accepted 14 November 2019
Available online 23 November 2019
0167-2738/

Abbreviations

BE	binding energy
DFT	density functional theory
MD	molecular dynamics
PAW	projector augmented wave
R-P	Ruddlesden–Popper
SOFC	solid oxide fuel cell
TEC	thermal expansion coefficient
TPD	temperature programmed desorption
UHV	ultra-high vacuum
VASP	Vienna Ab-initio Simulation Package
XPS	X-ray photoelectron spectroscopy

Nomenclature and units

a, b, c	unit cell parameters
D^*	oxygen tracer diffusion coefficient
e	charge of electron
$P(CO_2)$	carbon dioxide partial pressure
$P(O_2)$	oxygen partial pressure
V	unit cell volume
x	doping level in $Pr_{2-x}Ca_xNiO_{4+\delta}$
δ	oxygen overstoichiometry
1 Å	10^{-10} m
1 bar	10^5 Pa
1 e	$-1.602176634 \cdot 10^{-19}$ C
1 eV	96,485,33,289 J/mol

mechanism [30], cooperative interstitialcy mechanism [31] or interstitialcy-mediated mechanism [36]) as mentioned above involving lattice oxygen of perovskite layers and highly mobile interstitial oxygen of rock salt layers with the second one being able to be accumulated in a large amount [23,30,31,36,38,39,41,42]. The interstitial oxygen anions pass through the Ln_3 triangles to displace the apical oxygen anions of the NiO_6 octahedra, which move through the neighboring Ln_3 triangle to occupy the interstitial places. As demonstrated by MD for $La_{2-x}Sr_xCoO_{4\pm\delta}$ [31], extensive local relaxation occurs around interstitial position of oxygen anions consisting generally in the partial tilting of the adjacent CoO_6 octahedra to displace the neighboring oxygen anions. Relatively low migration barrier is caused by cooperative motion of polyhedra [30]. Calculated values of the migration barrier for this mechanism were reported to be in the range of 0.73–0.80 eV for $La_2CoO_{4+\delta}$, 0.71 eV for $La_{1.2}Sr_{0.8}CoO_{4.1}$ and 0.3–0.7 eV for $La_{2-x}Sr_xNiO_{4+\delta}$ which agree with the oxygen diffusion activation energy values according to the isotope exchange data [30,31,36]. It was reported that the interstitial oxygen anions can be both O^{2-} and O^- with migration of the last one being more energetically favorable [41], and interstitial peroxide anions being more stable than the oxide ones (as demonstrated for $La_{1.85}Sr_{0.15}CuO_{4+\delta}$ [40]). On the other hand, other authors reported that charge for both regular and interstitial oxygen varies not significantly, so there would be incorrect to separate "O^{2-}" and "O^-" anions (e.g., Bader charge for both regular and interstitial oxygen was calculated as $-1.34\ e$ – $-1.24\ e$ for $La_2CoO_{4+\delta}$) [30].

There is a difference in the oxygen transport trends at high and low temperatures [32]. At high temperatures, the oxygen transport is thermally activated, while it is lattice activated at low temperatures. According to the low-temperature diffusion simulation for $Nd_2NiO_{4+\delta}$ (δ = 0, 0.1 and 0.25), vibrational modes with [100] displacement and [110] delocalization allow exchange between interstitial and apical oxygen. At ambient temperature, increasing δ increases Ni cations effective charge leading to shortening Ni—O bonds and widening rock salt layers being filled by higher amounts of interstitial oxygen. At temperatures above 800 K δ effect on the oxygen mobility was not demonstrated [26,32].

Cooperative mechanism of oxygen migration can also involve oxygen vacancies in apical sites [36,40]. Interstitial oxide anion formation energy is lower in oxidizing conditions, while the vacancy formation energy is lower in reducing conditions [40]. According to DFT calculations for $La_{1.85}Sr_{0.15}CuO_{4+\delta}$, equatorial oxygen vacancies are more stable compared to apical ones [40]. According to MD calculations [31], for a high dopant content (e.g., for $LaSrCoO_{4\pm\delta}$) oxygen vacancies in perovskite layers are preferred to form in the equatorial plane (on O1 sites). It was also reported that, according to DFT calculation, decreasing oxygen vacancies formation energy leads to increasing the oxygen diffusivity [39]. Oxygen vacancy transport was simulated by MD for O-deficient $LaSrCoO_{4-\delta}$ [31]. According to these calculations, vacancies can migrate between two neighboring equatorial positions (path O1-O1, migration barrier 0.97 eV), between apical and equatorial positions (O2-O1, 1.14 eV) as well as hop between apical (O2-O2, 2.11 eV) and equatorial (O1-O1, 6.02 eV) positions of adjacent CoO_6 octahedra and even between neighboring perovskite layers (O2-O2, 1.26 eV). Thus, the lowest energy is for the vacancy migration pathway via adjacent equatorial positions along the octahedron edge within *a-b* plane, while apical-equatorial and apical-apical pathways are relatively favorable as well. Scatter plots demonstrate that exchange of oxygen anions between crystallographically nonequivalent O1 and O2 position occurs within *a-b* plane of perovskite layers in the case of oxygen vacancies presence. It is to be noted that oxygen vacancy migration along equatorial sites in perovskite layers is more favorable pathway for $La_2CuO_{4+\delta}$ compared to the interstitial oxygen migration [42,43]. The dominant defect type in anion sublattice of $La_{1.85}Sr_{0.15}CuO_{4+\delta}$ was reported to be equatorial vacancy [40].

In authors' previous study of features of oxygen transport in $Ln_{2-x}Ca_xNiO_{4+\delta}$ (Ln = La, Pr) [24], incorporation of oxygen into the interstitial position with a tetrahedral local Ln_4 environment and formation of four new O—Ln bonds was demonstrated to be most likely accompanied by a considerable weakening of two bonds of Ln cations with oxygen ions in the regular positions, which are even broken passing into the interstitial positions, which is in agreement with the cooperative mechanism of oxygen migration. Doping by alkaline earth metals such as Ca leads to a decrease of oxygen diffusivity resulting in some cases in emergence of 1–2 additional channels of slow oxygen migration. This can be hypothetically attributed to decreasing highly mobile interstitial oxygen content and steric hindrances while jumping through $Ln_{3-x}M_x$ cations' triangles [19,20,24].

The second possible mechanism of oxygen migration (*interstitial mechanism*) involves interstitial oxygen anions only [30]. According to this mechanism, the interstitial oxygen anion hops to adjacent interstitial site directly within *a-b* plane. However, according to both DFT and MD calculations this mechanism is less favorable. For $La_2CoO_{4+\delta}$ the migration barrier was reported to be 1.27–1.39 eV (compared to 0.73–0.80 eV for cooperative mechanism involving interstitials). This is due to absence of the cooperative motion of polyhedra and a higher charge density along the migration pathway for the interstitial mechanism [30].

The other mechanism being referred to as *oxide-peroxide mechanism* proposed for first R-P homologues considers involving both oxide (O^{2-}) and peroxide ($(O_2)^{2-}$) anions (which are also can be labelled as "O^-") with migration barrier for peroxide anions being lower compared to that for oxide ones or higher in some cases [36,41,44]. The distance between O atoms in such anions was calculated as 1.5–1.7 Å. The peroxide anions are stable or metastable dumbbells consisting of one interstitial and one apical oxygen anions. This mechanism (also called kick-out mechanism) includes association of metastable peroxide anions, pull out of apical oxygen and dissociation of peroxide anions

[36,44]. E.g., according to DFT calculations for $La_{2-x}Sr_xNiO_{4+\delta}$, migration barrier for this mechanism varies in the range of 0.5–3 eV depending on Ni cations charge compared to 0.3–0.7 eV for cooperative mechanism (the values are close and even value for oxide-peroxide mechanism is slightly lower for Ni cations charge of 2.5+) [36].

Moreover, there is a certain anisotropy in the oxygen transport: oxygen anions diffusion in *a-b* plane is faster than along the *c* axis, significant difference in calculated values of both diffusion coefficient and its effective activation energy being reported [23,25–27,31–34,43–49]. For undoped $Ln_2NiO_{4+\delta}$, it was demonstrated that octahedral rotations in the structure affect the interstitial oxygen transport in *I4/mmm* structure with the force constant of these rotations becoming "softer" with decreasing the Ln cation radius (with a minimum for Ln = Gd) [23]. A decrease in the Ln cation radius leads also to decreasing the cell volume and the migration barrier (with a minimum also for Ln = Gd) [23].

In this work characteristics of oxygen diffusion in $Pr_{2-x}Ca_xNiO_{4+\delta}$ (x = 0–0.6) estimated in authors' previous works by the oxygen isotope heteroexchange with $C^{18}O_2$ in the flow reactor [19] and O_2 thermoprogrammed desorption (TPD) [16] are compared with the results of surface analysis by XPS and modeling of the interstitial oxygen migration by plane-wave DFT calculations using VASP software.

2. Materials and methods

$Pr_{2-x}Ca_xNiO_{4+\delta}$ oxides (x = 0–0.6) were synthesized by a modified co-precipitation method. Cations content in starting materials Pr $(NO_3)_3{\cdot}xH_2O$, Ni$(NO_3)_2{\cdot}xH_2O$, and Ca$(NO_3)_2{\cdot}xH_2O$ with a purity of 99.96% were determined by an inductively coupled plasma optical emission spectroscopy using an Optima 4300 DV device. Taken in the stoichiometric ratio, nitrates were dissolved in a mixture of distilled water and ethanol (50:50) under continuous stirring and heating up to 70 °C. Then an excess of NH_4OH was added gradually to obtain a homogeneous gel of a blue-green color. Since the as-obtained gel contained soluble Ni complex ammines, it was taken for the subsequent treatment without washing to avoid Ni loss. After drying at 200 °C, a solid residue was thoroughly grinded in an agate mortar and calcined at 600 °C for 2 h. The black-colored powder was milled for 1 h using a Pulverisette-6 planetary mill (in agate drums, with the powder: stainless-steel balls: ethanol weight ratio of 1:5:1) and sintered first at 1150 °C for 5 h and, after subsequent milling for 1 h in the mill and drying, at 1250 °C for 10 h. For some compositions the last stage of synthesis was repeated to provide single-phase materials [20].

X-ray photoelectron spectra (XPS) were recorded using a SPECS spectrometer (Germany) with a PHOIBOS-150 hemispherical energy analyzer and AlK_α radiation ($h\nu$ = 1486.6 eV, 200 W). The binding energy scale was preliminarily calibrated using the peak positions of the $Au4f_{7/2}$ (84.0 eV) and $Cu2p_{3/2}$ (932.67 eV) core levels. The internal reference method was used for the correct calibration of the photoelectron peaks. The C1s peak (with binding energy of 284.8 eV) corresponded to the surface hydrocarbon-like deposits accumulated on the surface during storage under contact with atmosphere. Analysis of the data obtained by XPS was carried out by the software of XPS Peak 4.1. The spectra were curve-fitted after a Shirley (Shirley + Linear for Ni2p line) background subtraction. The line-shape was assumed to be a mixture of Gaussian and Lorentzian functions.

The oxygen treatment of $Pr_{1.6}Ca_{0.4}NiO_{4+\delta}$ sample was performed in a chamber of photoelectron spectrometer equipped with a special high-pressure cell allowing to made pretreatments of samples under different atmospheres at pressures up to 1 bar in the temperature range from 50 to 450 °C. In this case, sample was supported on the stainless-steel mesh spot welded to the standard sample holder. The oxygen treatment was performed for 1 h at $P(O_2) \sim 300$ mbar and temperature 350 °C, then sample was cooled down to room temperature and oxygen was pumped out from the cell (to UHV conditions – the background pressure $\sim 5 \times 10^{-8}$ mbar). Finally, after the oxygen pretreatment the sample was transferred to analyzer chamber without contact with air. The annealing of the $Pr_{1.6}Ca_{0.4}NiO_{4+\delta}$ sample in UHV at 500 °C was performed in the Preparation chamber where background pressure did not exceed 1×10^{-9} mbar.

DFT calculations: Migration of interstitial oxygen in the $Pr_{2-x}Ca_xNiO_{4+\delta}$ was studied within the plane-wave density functional theory. The Perdew–Burke–Ernzerhof (PBE) exchange-correlation functional was applied for the calculations. Valence electrons states were expanded in the plane waves with the 520 eV energy cut off. The interaction of valence electrons with cationic cores was modeled by the projector augmented wave (PAW) method. Brillouin zone was sampled with a mesh of 4 × 4 × 2 *k* points. The calculations were performed with account of antiferromagnetic binding of the magnetic moments of Ni cations using the VASP package [50,51]. The oxide in question was modeled by the 2 × 2 × 1 supercell (composed of 16 Pr, 8 Ni, 32 O atoms)/Additional (interstitial) oxygen atom was placed in the tetrahedral hollow site between the Pr cations. Energy and force convergence parameters were set to 0.1 meV and 0.1 meV/Å, respectively.

3. Results and discussion

3.1. X-ray diffraction

$Pr_{2-x}Ca_xNiO_{4+\delta}$ (x = 0–0.6) were single phase R-P oxides. Undoped $Pr_2NiO_{4+\delta}$ and samples with a low (x = 0.1) and high ($x \geq 0.4$) Ca content are crystallized in an orthorhombic structure (*O*, Table 1) with a *Fmmm* space group at low temperatures and a *I4/mmm* space group at high temperatures. Unit cell parameters and volume for the orthorhombic structure as well as parameters and volume recalculated to orthorhombic ones for the tetragonal structure decrease with Ca content, which can be assigned to lowering the interstitial oxygen content due to charge compensation. The samples with an intermediate Ca content (x = 0.2–0.3) retain a tetragonal structure (*T*) with an *I4/mmm* space group over the entire temperature range (25–850 °C). This orthorhombic – tetragonal structure transition is related to decreasing the interstitial oxygen content. The low-temperature modification of samples with a high dopant content can be also attributed to *Bbcm* space group. Orthorhombic – tetragonal structure transition is probably related with the Jahn – Teller Ni^{3+} cations' content increasing [19]. Results of XRD studies are summarized in Table 1. According to in situ XRD studies using synchrotron radiation, the phase transitions *Fmmm* ↔ *I4/mmm* were observed related with the temperature increase and the oxygen loss. These phase transitions are reversible in air atmosphere. The temperature of this transition varies

Table 1
Crystal structure and unit cell parameters for $Pr_{2-x}Ca_xNiO_{4+\delta}$ oxides.

x	0.0	0.1	0.2	0.3	0.4	0.5	0.6
Structure	*O*	*O*	*T*	*T*	*O*	*O*	*O*
Space group	*Fmmm*	*Fmmm*	*I4/mmm*	*I4/mmm*	*Bbcm*	*Bbcm*	*Bbcm*
a, [Å]	5.3923 (2)	5.3864(2)	3.8129(1)	3.8044(1)	5.3737(1)	5.3373(1)	5.3451(1)
b, [Å]	5.4610(2)	5.4293(2)	3.8129(1)	3.8044(1)	5.3531(1)	5.3590(1)	5.3716(1)
c, [Å]	12.4441(5)	12.4258(4)	12.4089(2)	12.3900(2)	12.3619(3)	12.3590(4)	12.3603(3)
V, [Å^3]	366.45(2)	363.39(2)	180.404(4)	179.322(5)	355.61(1)	353.50(2)	354.89(1)

depending on Ca content non-monotonously. The detailed discussion of structure features elucidated using XRD data analysis is omitted for brevity and can be found in authors' previous works [19,20].

The evolution of the structure with an increase in calcium content is associated with a decrease in content of the over-stoichiometric oxygen with doping. This fact was experimentally revealed by the TGA and iodometric titration methods [19,20,22]. It was shown that for $Pr_{2-x}Ca_xNiO_{4+\delta}$ samples with $x = 0$, 0.2 and 0.4, for which the structural changes were observed, the over-stoichiometric oxygen content (δ) changed in the row 0.25, 0.11 and 0.02, respectively. The δ value for the sample with the maximum doping level ($x = 0.6$) was low (0.008), but still positive [20]. The δ value may change with both temperature [15,20,52] and oxygen partial pressure variation [53], which also may cause phase transitions. In the case of undoped $Pr_2NiO_{4+\delta}$ the reversible orthorhombic (*Fmmm*) → tetragonal (*I4/mmm*) phase transition is observed in the temperature range of 400–500 °C depending on samples' pre-history and ambient conditions. The weight loss caused by the oxygen release from the layered structure of $Pr_{2-x}Ca_xNiO_{4+\delta}$ under heating decreases at $x \geq 0.2$, which results in the structural stabilization over the entire temperature range from the room temperature up to SOFC operating temperatures [20].

3.2. X-ray photoelectron spectroscopy

XPS spectra measured for the fresh and after different treatments $Pr_{1.6}Ca_{0.4}NiO_{4+\delta}$ sample are presented in Figs. 1–3. One can see that for the fresh sample Ni is present in two states with binding energies (BE) of $Ni2p_{3/2}$ of 854.7 and 856.2 eV (Fig. 1(a)), which could be assigned to the Ni^{2+} in $Pr_{1.6}Ca_{0.4}NiO_{4+\delta}$ and Ni^{2+} in $Ni(OH)_2$, respectively [6,54,55]. We believe that the latter state is more preferable than Ni^{3+} in the composition of Ni_2O_3. Indeed, Greiner et al. [56] suggested the formation of $Ni(OH)_2$ rather than Ni_2O_3 on the NiO surface, which was attributed to the higher thermodynamic stability of $Ni(OH)_2$ compared with Ni_2O_3. Consistent with this hypothesis, Seo et al. [57] reported the formation of $Ni(OH)_2$ on a carbon fiber Ni film rather than Ni_2O_3 as well.

After annealing in vacuum at 500 °C the state attributed to $Ni(OH)_2$ fully disappeared and only Ni^{2+} in $Pr_{1.6}Ca_{0.4}NiO_{4+\delta}$ is present. For all subsequent treatments the Ni2p spectra remained unchanged. The binding energy value of $Pr3d_{5/2}$ is 933.1 eV which is typical for Pr^{3+} state (Fig. 1(b)) [58], the shape and position of Pr3d spectra did not change depending on the sample treatments. For the initial sample Ca is in two states with BE values of 346.5 and 347.5 eV (Fig. 2(a)), which were attributed to Ca^{2+} state in $Pr_{1.6}Ca_{0.4}NiO_{4+\delta}$ and Ca^{2+} in $CaCO_3$ [6,59,60]. The presence of $CaCO_3$ was also confirmed by the C1s spectra of fresh sample (Fig. 2(b)), where the pronounced peak at 289.3 eV exists, which is typical for carbonates on the surface. The annealing of the sample leads to the disappearance of peaks assigned to carbonates for both Ca2p and C1s spectra. As for the case of Ni2p further treatments did not change the shape and positions of the Ca2p and C1s XPS spectra. Fig. 3 shows the O1s XPS spectra measured for $Pr_{1.6}Ca_{0.4}NiO_{4+\delta}$ before and after different treatments (Table 2). For the fresh sample, the O1s peak at the binding energy of 529.1 eV can be assigned to the lattice oxygen O^{2-} in the perovskite layers of the R-P structure. The peak at 530.8 ± 0.1 eV is related to the weakly bound oxygen, while the peak with the BE value of 532.0 ± 0.2 eV can be attributed to the oxygen in the surface hydroxyl/carbonate groups ($Ni(OH)_2$ and $CaCO_3$). In order to reveal the validity of the assignment of the peak at the binding energy of ~531 eV to the weakly bound oxygen, the sample $Pr_{1.6}Ca_{0.4}NiO_{4+\delta}$ was heated in UHV (ultra-high vacuum condition) up to 500 °C. A decrease in the intensity of this peak indicates that it corresponds to the weakly bound oxygen species, whereas the intensity of the peak at ~529 eV, related to the lattice oxygen, remains practically unchanged.

The ratio of peaks intensities of the weakly bound oxygen to the lattice one decreases from 0.5 to 0.4 (see Table 2). One can see as well that after heating in UHV at 500 °C the peak attributed to hydroxyls and carbonate groups almost disappeared (Fig. 2). Treatment in oxygen at 350 °C ($P(O_2) = 300$ mbar, $t = 1$ h) leads to the recovering of weakly bound oxygen intensity, the peak intensities ratio between O1s peaks at 530.8 eV and 529.1 eV increased from 0.4 to 0.54. The second heating in vacuum at 500 °C again leads to decreasing of this ratio to 0.38, i.e. to the ratio obtained after the first heating (Table 2). These data allow us to conclude that the weakly bound oxygen has the relatively high mobility.

It is to be noted that removal temperature of weakly bound oxygen correlates with temperature of the interstitial oxygen desorption according to TPD O_2 (400–600 °C) demonstrating the intense peak of the excess oxygen removal from rock-salt layers [16]. Two types of oxygen anions according to O1s XPS data (lattice and weakly bound) might be also in agreement with TPIE data showing nonuniformity of bulk oxygen demonstrated as slow and fast diffusion channels (Section 3.3).

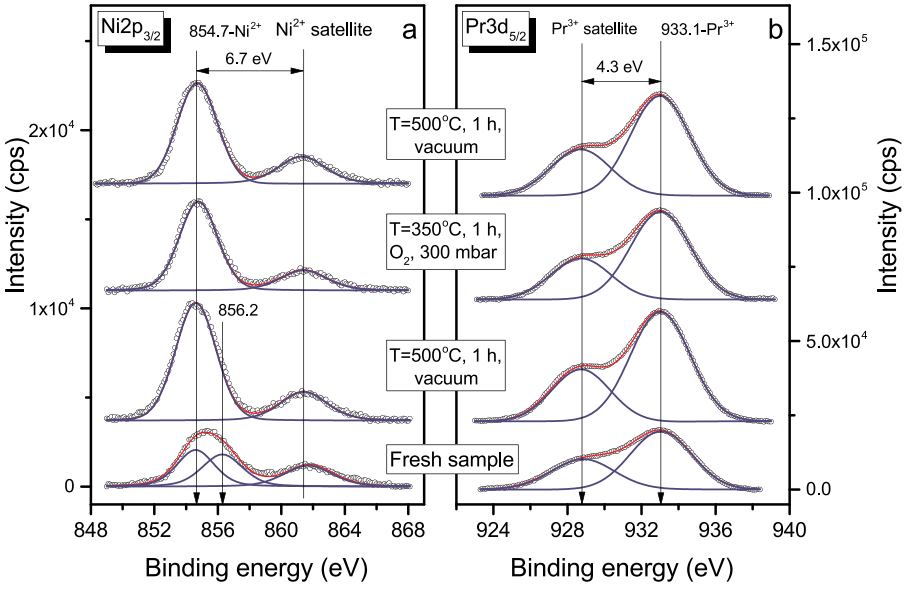

Fig. 1. $Ni2p_{3/2}$ (a) and $Pr3d_{5/2}$ (b) XPS spectra of $Pr_{1.6}Ca_{0.4}NiO_{4+\delta}$ sample.

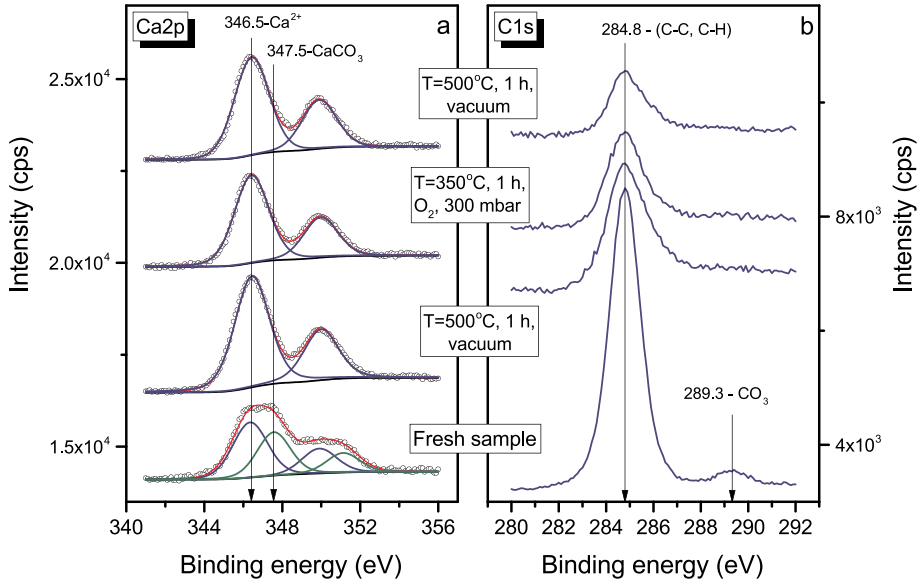

Fig. 2. Ca2p (a) and C1s (b) XPS spectra of $Pr_{1.6}Ca_{0.4}NiO_{4+\delta}$ sample.

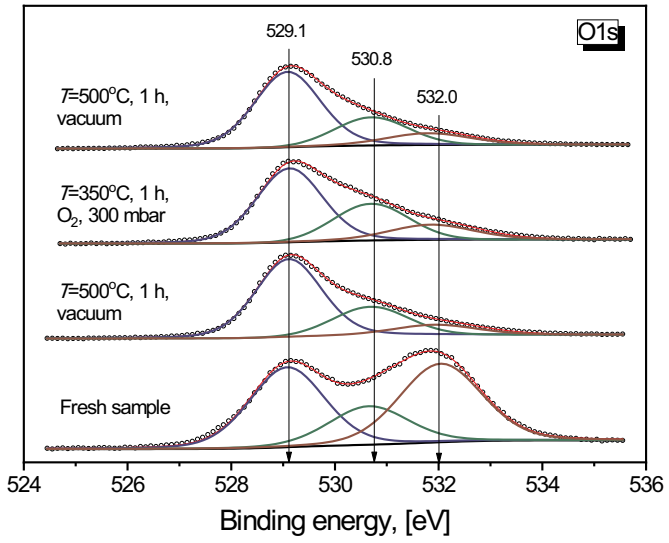

Fig. 3. O1s XPS spectra of $Pr_{1.6}Ca_{0.4}NiO_{4+\delta}$ at different sample treatment.

3.3. Isotope exchange data

Oxygen transport features of $Pr_{2-x}Ca_xNiO_{4+\delta}$ were studied by the temperature programmed isotope exchange of oxygen with $C^{18}O_2$ in a flow reactor [19]. According to the isotope exchange data, the oxygen mobility is high (tracer diffusion coefficient values are $\sim 10^{-10}$–10^{-7} cm^2/s at 700 °C depending on composition). This is explained by cooperative mechanism of oxygen migration involving both regular and interstitial oxygen described above in the Introduction. Doping with Ca^{2+} having a larger radius compared to Pr^{3+} [61] results in decreasing the oxygen diffusivity. At the dopant content $x \geq 0.4$ it leads to forming 1–2 additional channels of oxygen migration with complicated diffusion (Table 3). This can be explained by decreasing the highly-mobile interstitial oxygen content as well as steric hindrances while passing the interstitial oxygen anions through the $Pr_{3-x}Ca_x$ triangles. Details can be found in authors' previous work devoted to oxygen transport studies in $Pr_{2-x}Ca_xNiO_{4+\delta}$ [19]. Oxygen transport properties of Ca-doped $Pr_2NiO_{4+\delta}$ obtained by the authors of this work as well as the data on the oxygen transport properties of $Pr_2NiO_{4+\delta}$, obtained by other methods, are summarized in Table 3. The data on oxygen diffusion in $Pr_2NiO_{4+\delta}$, obtained in this study agree well with those obtained in [15]. Anisotropy of mobility of oxygen interstitials, migrating by an interstitial (or push − pull) mechanism in the rock-salt layers was evidenced by the experimental data obtained in [40] using measurement on a single crystal and revealed by MD simulations made in [26]. The authors [26] argue that the migration takes place mainly in the *a-b* plane and depends upon the degree of over-stoichiometry. Calculated values of the activation energy for the oxygen diffusion process changed from 0.49 eV ($\delta = 0.025$) to 0.64 eV ($\delta = 0.20$). Dependence of the oxygen migration barriers, calculated by MD method, on the oxygen interstitial concentration was also demonstrated in [23]. It was found that the migration barrier value changes from 0.535 eV at $\delta = 0.065$ to 0.915 eV at $\delta = 0.125$.

The value of activation energy found for undoped $Pr_2NiO_{4+\delta}$ [19] (Table 3) lies within the range of those calculated in the works [23,26]. Doping with Ca up to $Pr_{1.7}Ca_{0.3}NiO_{4+\delta}$ composition results in activation energy values slightly exceeding this range. However, calculations from isotope exchange data presented in authors' previous work [19] agree in general with those presented in the works [23,26]. With increasing Ca content the effective activation energy values increase, which might be related with transport features discussed above.

Table 2
The contribution (in [%]) of the oxygen states peaks to the total O1s spectra at different sample treatments.

Sample/treatment conditions	529.1 eV lattice	530.8 eV weakly bonded	532 eV hydroxyls/carbonates	530.8/529.1 ratio
Fresh sample	38.9	19.6	41.5	0.50
Treatment in vacuum, 500 °C, 1 h	64.0	25.4	10.6	0.40
Treatment in O_2, 350 °C, P = 300 mbar, 1 h	55.6	30.1	14.3	0.54
Second treatment in vacuum, 500 °C, 1 h	64.1	24.4	11.5	0.38

Table 3
Experimental values of oxygen tracer diffusion coefficients at 700 °C for the $Pr_2NiO_{4+\delta}$–based materials (the data were extracted from the graphic materials presented in [10,15,19,46] using OriginPro tools) and apparent activation energy for the oxygen diffusion process obtained by different methods.[b,c]

Composition	$D^*\|_{700°C}$, [cm^2/s]	Apparent activation energy, [eV]	Technique of measurements/calculations	$P(O_2/CO_2)$, [bar]	Reference
$Pr_2NiO_{4+\delta}$	$7.0 \cdot 10^{-8}$	0.83	TPIE ($C^{18}O_2$)[a]	0.01	[19]
$Pr_{1.9}Ca_{0.1}NiO_{4+\delta}$	$3.4 \cdot 10^{-9}$	1.08	TPIE ($C^{18}O_2$)	0.01	[19]
$Pr_{1.7}Ca_{0.3}NiO_{4+\delta}$	$7.6 \cdot 10^{-10}$	0.93	TPIE ($C^{18}O_2$)	0.01	[19]
$Pr_{1.6}Ca_{0.4}NiO_{4+\delta}$	$6.1 \cdot 10^{-10}$ (fast) $1.6 \cdot 10^{-12}$ (slow)	1.45 (fast) 1.66 (slow)	TPIE ($C^{18}O_2$)	0.01	[19]
$Pr_2NiO_{4+\delta}$	$6.33 \cdot 10^{-8}$	0.71	SIMS[b] (^{18}O)	0.21	[15]
$Pr_2NiO_{4+\delta}$	$3.12 \cdot 10^{-9}$	2.0	GPE[c] (^{18}O)	0.007	[10]
$Pr_2NiO_{4+\delta}$ (*a-b* plane)	$1.13 \cdot 10^{-7}$	0.67	SIMS (^{18}O)	0.21	[46]
$Pr_2NiO_{4+\delta}$ (*c* axis)	$5.86 \cdot 10^{-10}$	1.10	SIMS (^{18}O)	0.21	[46]

[a] TPIE – temperature programmed isotope exchange.
[b] SIMS – secondary ion mass spectrometry.
[c] GPE – isotope exchange with gas phase equilibration.

3.4. DFT calculations

Migration of interstitial oxygen was modeled for the *I4/mmm* phase of $Pr_2NiO_{4+\delta}$ [20] (Fig. 4) with antiferromagnetic binding of the magnetic moments of Ni cations (unlike the work by Aspera et al. [34]).

The $Pr_2NiO_{4+\delta}$ structure obtained with $\delta = 1/32 = 0.031$ appears to be significantly distorted compared to the initial one without interstitial oxygen (Fig. 5(a)). The interstitial oxygen anion repulses the apical oxygen in the NiO_6 octahedra even in the initial state (both anions are marked pink in Fig. 5(b)). In the transition state, the interstitial oxygen anion forces the apical one to break Ni—O coordination bond, so both anions are placed at a long distance of 3.3 Å to the Ni cation as compared to undistorted Ni—O bond length of about 2.0 Å (Fig. 5(b)). Further approaching leads to pushing the apical anion into the tetrahedral hollow site between Pr cations (Fig. 5(c)). The Bader charge [62] of these anions was equal to −1.2 *e*. The activation barrier of this migration was 0.585 eV according to the calculations using NEB method, which agrees with the experimental value of 0.83 eV (Table 3). Note that earlier estimations using the interacting bonds semi-empirical method provided underestimated value of the migration barrier of about 0.3 eV [16], while molecular dynamics simulations overestimated it (up to 1.2 eV) [23].

Complete substitution of Pr cations by Ca dramatically changes interaction between lattice and interstitial oxygen centers. Nonstoichiometric oxygen (1 per 4 unit cells) in the structure of $Ca_2NiO_{4+\delta}$ is attached to the oxygen ion in a regular lattice position with the formation of peroxide ion $(O_2)^{2-}$ species with the O—O distance of 1.39 Å (Fig. 6). The peroxide structure also manifests itself in almost identical Bader oxygen charges of −0.51 *e* and −0.56 *e* for lattice and interstitial oxygen ions, respectively, despite their nonequivalent positions in the unit cell. Note that for other lattice oxygen ions the Bader charges are in the range of −1.2 *e* to −0.98 *e*. For the half-and-half Pr—Ca substitution (the $PrCaNiO_{4+\delta}$ structure), the formation of peroxide does not take place. In fact, $Pr_2NiO_{4+\delta}$-like structures were obtained in this case. Hence, DFT calculations provide realistic estimation of the oxygen migration barriers in doped Pr nickelate with R-P structure explaining observed trends in oxygen mobility (Table 3).

4. Conclusions

Transport properties of Ca-doped $Pr_2NiO_{4+\delta}$ in connection with structure features and ions' state were studied. Weakly bound oxygen presence was proved. DFT calculations provide realistic estimation of the oxygen migration barriers explaining observed trends in oxygen mobility. The materials studied are promising for using in SOFC

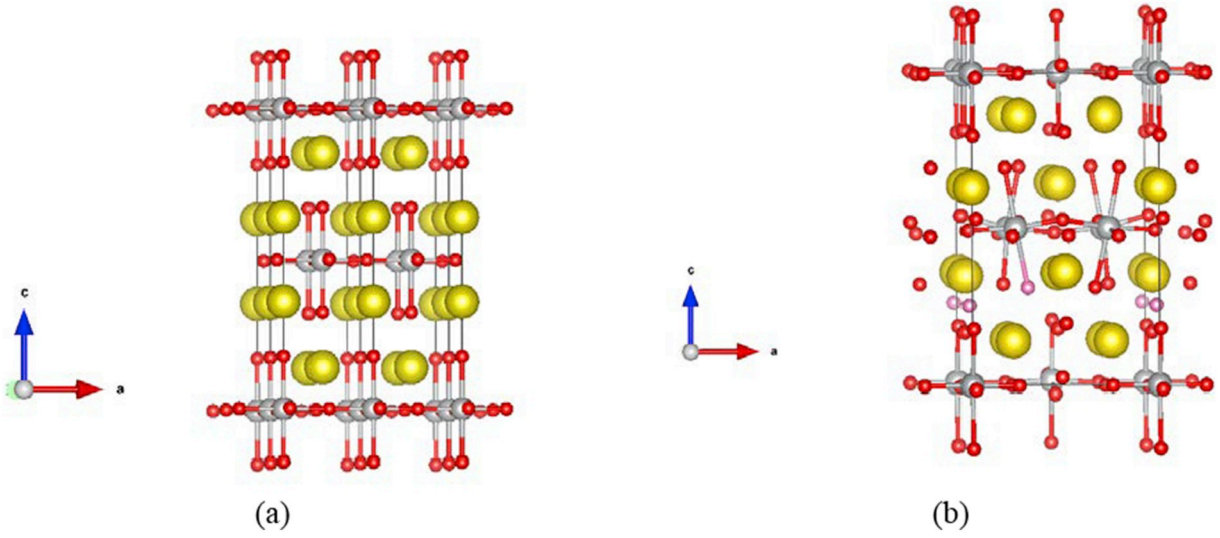

Fig. 4. The initial 2 × 2 × 1 *I4/mmm* supercell for $Pr_2NiO_{4+\delta}$ (a) and the same unit cell with 1 additional interstitial oxygen anion after geometry optimization. Colors: Pr – yellow, Ni – grey, O – red (interstitial and apical oxygen anions are marked pink). (For interpretation of the references to color in this figure legend, the reader is referred to the web version of this article.)

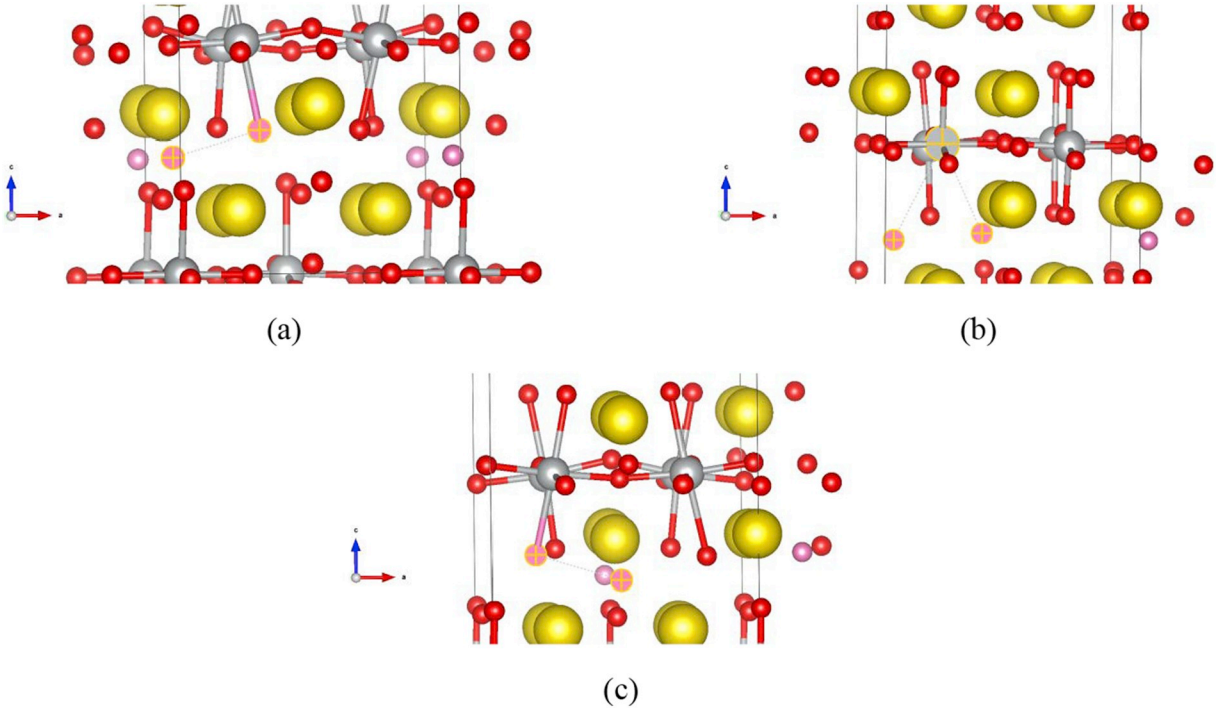

Fig. 5. Initial (a), intermediate (b) and final (c) state of the interstitial and apical oxygen anions (pink). (For interpretation of the references to color in this figure legend, the reader is referred to the web version of this article.)

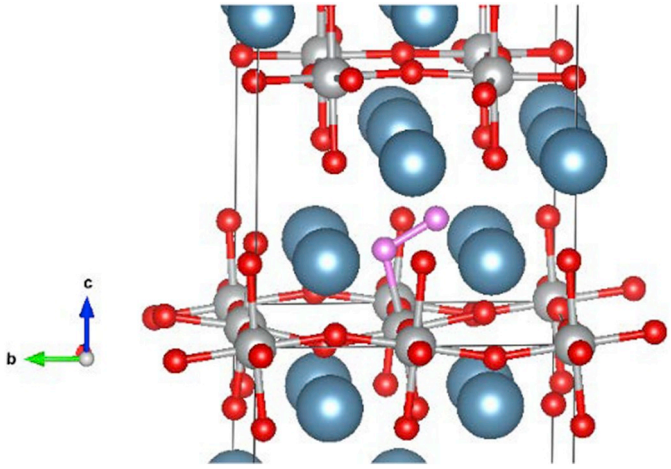

Fig. 6. Formation of peroxide ion structure (highlighted in pink) in case of complete substitution of Pr by Ca (blue). (For interpretation of the references to color in this figure legend, the reader is referred to the web version of this article.)

cathodes and permselective layers of oxygen separation membranes.

Acknowledgements

Authors would like to give acknowledgement to 22nd International Conference on Solid State Ionics (SSI-22) Organization Committee.

Funding

Support by Russian Science Foundation (Project 16-13-00112) is gratefully acknowledged.

Declaration of competing interest

None.

References

[1] J. Dailly, S. Fourcade, A. Largeteau, F. Mauvy, J.C. Grenier, M. Marrony, Perovskite and A_2MO_4-type oxides as new cathode materials for protonic solid oxide fuel cells, Electrochim. Acta 55 (20) (2010) 5847–5853, https://doi.org/10.1016/j.electacta.2010.05.034.

[2] C. Ferchaud, J.-C. Grenier, Y. Zhang-Steenwinkel, M.M.A. van Tuel, F.P.F. van Berkel, J.-M. Bassat, High performance praseodymium nickelate oxide cathode for low temperature solid oxide fuel cell, J. Power Sources 196 (4) (2011) 1872–1879, https://doi.org/10.1016/j.jpowsour.2010.09.036.

[3] X.-D. Zhou, J.W. Templeton, Z. Nie, H. Chen, J.W. Stevenson, L.R. Pederson, Electrochemical performance and stability of the cathode for solid oxide fuel cells: V. high performance and stable Pr_2NiO_4 as the cathode for solid oxide fuel cells, Electrochim. Acta 71 (2012) 44–49, https://doi.org/10.1016/j.electacta.2012.03.067.

[4] P. Batocchi, F. Mauvy, S. Fourcade, M. Parco, Electrical and electrochemical properties of architectured electrodes based on perovskite and A_2MO_4-type oxides for Protonic ceramic fuel, Cell, Electrochim. Acta 145 (2014) 1–10, https://doi.org/10.1016/j.electacta.2014.07.001.

[5] B. Philippeau, F. Mauvy, C. Mazataud, S. Fourcade, J.-C. Grenier, Comparative study of electrochemical properties of mixed conducting $Ln_2NiO_{4+\delta}$ (Ln = La, Pr and Nd) and $La_{0.6}Sr_{0.4}Fe_{0.8}Co_{0.2}O_{3-\delta}$ as SOFC cathodes associated to $Ce_{0.9}Gd_{0.1}O_{2-\delta}$, $La_{0.8}Sr_{0.2}Ga_{0.8}Mg_{0.2}O_{3-\delta}$ and $La_9Sr_1Si_6O_{26.5}$ electrolytes, Solid State Ionics 249 (2013) 17–25, https://doi.org/10.1016/j.ssi.2013.06.009.

[6] E. Pikalova, A. Kolchugin, N. Bogdanovich, D. Medvedev, J. Lyagaeva, L. Vedmid, M. Ananyev, S. Plaksin, A. Farlenkov, Suitability of $Pr_{2-x}Ca_xNiO_{4+\delta}$ as cathode materials for electrochemical devices based on oxygen ion and proton conducting solid state electrolytes, Int. J. Hydrog. Energy (2018), https://doi.org/10.1016/j.ijhydene.2018.06.023 In Press, corrected proof.

[7] X. Meng, S. Lü, S. Liu, X. Liu, Y. Sui, X. Li, M. Pang, B. Wang, Y. Ji, M.Z. Hu, Electrochemical characterization of B-site cation-excess $Pr_2Ni_{0.75}Cu_{0.25}Ga_{0.05}O_{4+\delta}$ cathode for IT-SOFCs, Ceram. Int. 41 (2015) 12107–12114, https://doi.org/10.1016/j.ceramint.2015.06.028.

[8] A. Tarutin, J. Lyagaeva, A. Farlenkov, S. Plaksin, G. Vdovin, A. Demin, D. Medvedev, A reversible protonic ceramic cell with symmetrically designed $Pr_2NiO_{4+\delta}$-based electrodes: fabrication and electrochemical features, Materials 12 (2019) 118, https://doi.org/10.3390/ma12010118.

[9] W. Li, B. Guan, L. Ma, S. Hu, N. Zhang, X. Liu, High performing triple-conductive $Pr_2NiO_{4+\delta}$ anode for proton-conducting steam solid oxide electrolysis cell, J. Mater. Chem. A 6 (37) (2018) 18057–18066, https://doi.org/10.1039/C8TA04018D.

[10] A.V. Kovalevsky, V.V. Kharton, A.A. Yaremchenko, Y.V. Pivak, E.V. Tsipis, S.O. Yakovlev, A.A. Markov, E.N. Naumovich, J.R. Frade, Oxygen permeability,

stability and electrochemical behavior of $Pr_2NiO_{4+\delta}$–based materials, Electroceram 18 (3–4) (2007) 205–218, https://doi.org/10.1007/s10832-007-9024-7.
[11] P.-M. Geffroy, M. Reichmann, T. Chartier, J.-M. Bassat, J.-C. Grenier, Evaluating oxygen diffusion, surface exchange and oxygen semi-permeation in $Ln_2NiO_{4+\delta}$ membranes (Ln = La, Pr and Nd), J. Memb. Sci. 451 (2014) 234–242, https://doi.org/10.1016/J.MEMSCI.2013.08.035.
[12] T. Ishichara, S. Miyoshi, T. Furuno, O. Sanguanruang, H. Matsumoto, Mixed conductivity and oxygen permeability of doped Pr_2NiO_4-based oxide, Solid State Ionics 177 (35–36) (2006) 3087–3091, https://doi.org/10.1016/j.ssi.2006.08.013.
[13] T. Ishichara, N. Sirikanda, K. Nakashima, S. Miyoshi, H. Matsumoto, Mixed oxide ion and hole conductivity in $Pr_{2-d}Ni_{0.76-x}Cu_{0.24}Ga_xO_{4+\delta}$ membrane, J. Electrochem. Soc. 157 (1) (2010) B141–B146, https://doi.org/10.1149/1.3251004.
[14] S. Miyoshi, T. Furuno, O. Sanguanruang, H. Matsumoto, T. Ishichara, Mixed conductivity and oxygen permeability of doped Pr_2NiO_4-based oxides, J. Electrochem. Soc. 157 (1) (2010) B141–B146, https://doi.org/10.1149/1.2387103.
[15] E. Boehm, J.-M. Bassat, P. Dordor, F. Muvy, J.-C. Grenier, Ph. Stevens, Oxygen diffusion and transport properties in non-stoichiometric $Ln_{2-x}NiO_{4+\delta}$ oxides, Solid State Ionics 176 (2005) 2717–2725, https://doi.org/10.1016/j.ssi.2005.
[16] V.A. Sadykov, N.F. Eremeev, V.V. Usol'tsev, A.S. Bobin, G.M. Alikina, V.V. Pelipenko, E.M. Sadovskaya, V.S. Muzykantov, N.N. Bulgakov, N.F. Uvarov, Mechanism of oxygen transfer in layered lanthanide nickelates $Ln_{2-x}NiO_{4+\delta}$ (Ln = La, Pr) and their nanocomposites with $Ce_{0.9}Gd_{0.1}O_{2-\delta}$ and $Y_2(Ti_{0.8}Zr_{0.2})_{1.6}Mn_{0.4}O_{7-\delta}$ solid electrolytes, Russ. J. Electrochem. 49 (2013) 645–651, https://doi.org/10.1134/S1023193513070136.
[17] N.M. Porotnikova, A.V. Khodimchuk, M.V. Ananyev, V.A. Eremin, E.S. Tropin, A.S. Farlenkov, E.Yu. Pikalova, A.V. Fetisov, Oxygen isotope exchange in praseodymium nickelate, J. Solid State Chem. 22 (7) (2018) 2115–2126, https://doi.org/10.1007/s10008-018-3919-x.
[18] E.Y. Pikalova, A.A. Kolchugin, V.A. Sadykov, E.M. Sadovskaya, E.A. Filonova, N.F. Eremeev, N.M. Bogdanovich, Structure, transport properties and electrochemical behavior of the layered lanthanide nickelates doped with calcium, Int. J. Hydrog. Energy 43 (36) (2018) 17373–17386, https://doi.org/10.1016/j.ijhydene.2018.07.115.
[19] V.A. Sadykov, E.Y. Pikalova, A.A. Kolchugin, E.A. Filonova, E.M. Sadovskaya, N.F. Eremeev, A.V. Ishchenko, A.V. Fetisov, S.M. Pikalov, Oxygen transport properties of Ca-doped Pr_2NiO_4, Solid State Ionics 317 (2018) 234–243, https://doi.org/10.1016/j.ssi.2018.01.035.
[20] V.A. Sadykov, E.Y. Pikalova, Z.S. Vinokurov, A.N. Shmakov, N.F. Eremeev, E.M. Sadovskaya, J.G. Lyagaeva, D.A. Medvedev, V.D. Belyaev, Tailoring the structural, thermal and transport properties of $Pr_2NiO_{4+\delta}$ through Ca-doping strategy, Solid State Ionics 333 (2019) 30–37, https://doi.org/10.1016/j.ssi.2019.01.014.
[21] P. Odier, Ch. Allançon, J.M. Bassat, Oxygen exchange in $Pr_2NiO_{4+\delta}$ at high temperature and direct formation of $Pr_4Ni_3O_{10-2x}$, J. Solid State Chem. 153 (2000) 381–385, https://doi.org/10.1006/jssc.2000.8786.
[22] E.Y. Pikalova, D.A. Medvedev, A.F. Khasanov, Structure, stability, and thermomechanical properties of Ca-substituted $Pr_2NiO_{4+\delta}$, Phys. Solid State 59 (4) (2017) 694–702, https://doi.org/10.1134/S1063783417040187.
[23] X. Li, N.A. Benedek, Enhancement of ionic transport in complex oxides through soft lattice modes and epitaxial strain, Chem. Mater. 27 (2015) 2647–2652, https://doi.org/10.1021/acs.chemmater.5b00445.
[24] V.A. Sadykov, E.M. Sadovskaya, E.Yu. Pikalova, A.A. Kolchugin, E.A. Filonova, S.M. Pikalov, N.F. Eremeev, A.V. Ishchenko, A.I. Lukashevich, J.M. Bassat, Transport features in layered nickelates: correlation between structure, oxygen diffusion, electrical and electrochemical properties, Ionics 24 (4) (2018) 1181–1193, https://doi.org/10.1007/s11581-017-2279-3.
[25] A. Chroneos, D. Parfitt, J.A. Kilner, R.W. Grimes, Anisotropic oxygen diffusion in tetragonal $La_2NiO_{4+\delta}$: molecular dynamics calculations, J. Mater. Chem. 20 (2) (2010) 266–270, https://doi.org/10.1039/B917118E.
[26] D. Parfitt, A. Chroneos, J.A. Kilner, R.W. Grimes, Molecular dynamics study of oxygen diffusion in $Pr_2NiO_{4+\delta}$, Phys. Chem. Chem. Phys. 12 (2010) 6834–6836, https://doi.org/10.1039/c001809k.
[27] G.N. Mazo, Y. Mamaev, M.Z. Galin, M.S. Kaluzhskikh, A.K. Ivanov-Schitz, Structural and transport properties of the layered cuprate Pr_2CuO_4, Inorg. Mater. 47 (2011) 1218–1226, https://doi.org/10.1134/S0020168511110136.
[28] G.N. Mazo, S.N. Savvin, The molecular dynamics study of oxygen mobility in $La_{2-x}Sr_xCuO_{4-\delta}$, Solid State Ionics 175 (2004) 371–374, https://doi.org/10.1016/j.ssi.2003.12.028.
[29] G.N. Mazo, M.Z. Galin, N.V. Lyskov, A.K. Ivanov-Schitz, Computer simulation of ion transport in a new cathode material $PrSrCuO_{4-\delta}$, Crystallogr. Rep. 59 (2) (2014) 252–257, https://doi.org/10.1134/S106377451402014X.
[30] A. Kushima, D. Parfitt, A. Chroneos, B. Yildiz, J.A. Kilner, R.W. Grimes, Interstitialcy diffusion of oxygen in tetragonal $La_2CoO_{4+\delta}$, Phys. Chem. Chem. Phys. 13(6) (2011) 2242–2249. https://doi.org/doi:https://doi.org/10.1039/c0cp01603a.
[31] C. Tealdi, C. Ferrara, P. Mustarelli, M.S. Islam, Vacancy and interstitial oxide ion migration in heavily doped $La_{2-x}Sr_xCoO_{4\pm\delta}$, J. Mater. Chem. 22 (18) (2012) 8969–8975, https://doi.org/10.1039/c2jm30769c.
[32] A. Perrichon, A. Piovano, M. Boehm, M. Zbiri, M. Johnson, H. Schober, M. Ceretti, W. Paulus, Lattice dynamics modified by excess oxygen in $Nd_2NiO_{4+\delta}$: triggering low-temperature oxygen diffusion, J. Phys. Chem. C 119 (3) (2015) 1557–1564, https://doi.org/10.1021/jp510392h.
[33] C. Frayret, A. Villesuzanne, M. Pouchard, Application of density functional theory to the modeling of the mixed ionic and electronic conductor $La_2NiO_{4+\delta}$: lattice relaxation, oxygen mobility, and energetics of Frenkel defects, Chem. Mater. 17 (2005) 6538–6544, https://doi.org/10.1021/cm050195f.
[34] S.M. Aspera, M. Sakaue, T.D.K. Wungu, M. Alaydrus, T.P.T. Linh, H. Kasai, M. Nakanishi, T. Ishihara, Analysis of structural and electronic properties of Pr_2NiO_4 through first-principles calculations, J. Phys. Condens. Matter 24 (2012) 405504–405514, https://doi.org/10.1088/0953-8984/24/40/405504.
[35] N. Zhou, G. Chen, H.J. Zhang, C. Zhou, Synthesis and transport properties of La_2NiO_4, Physica B 404 (2009) 4150–4154, https://doi.org/10.1016/j.physb.2009.07.186.
[36] S. Xu, R. Jacobs, D. Morgan, Factors controlling oxygen interstitial diffusion in the Ruddlesden–Popper oxide $La_{2-x}Sr_xNiO_{4+\delta}$, Chem. Mater. 30 (2) (2018) 7166–7177, https://doi.org/10.1021/acs.chemmater.8b03146.
[37] M. Yashima, H. Yamada, S. Nuansaeng, T. Ishihara, Role of Ga^{3+} and Cu^{2+} in the high interstitial oxide-ion diffusivity of Pr_2NiO_4-based oxides: design concept of interstitial ion conductors through the higher-valence d^{10} dopant and Jahn–Teller effect, Chem. Mater. 24 (21) (2012) 4100–4113, https://doi.org/10.1021/cm3021287.
[38] W. Xie, Y.-L. Lee, Y. Shao-Horn, D. Morgan, Oxygen point defect chemistry in Ruddlesden–Popper oxides $(La_{1-x}Sr_x)_2MO_{4\pm\delta}$ (M = Co, Ni, Cu), J. Phys. Chem. Lett. 7 (10) (2016) 1939–1944, https://doi.org/10.1021/acs.jpclett.6b00739.
[39] R.P. Forslund, W.G. Hardin, X. Rong, A.M. Abakumov, D. Filimonov, C.T. Alexander, J.T. Mefford, H. Iyer, A.M. Kolpak, K.P. Johnston, K.J. Stevenson, Exceptional electrocatalytic oxygen evolution via tunable charge transfer interactions in $La_{0.5}Sr_{1.5}Ni_{1-x}Fe_xO_{4\pm\delta}$ Ruddlesden-Popper oxides, Nat. Commun. 9 (2018) 3150, https://doi.org/10.1038/s41467-018-05600-y.
[40] T.L. Meyer, R. Jacobs, D. Lee, L. Jiang, J.W. Freeland, C. Sohn, T. Egami, D. Morgan, H.N. Lee, Strain control of oxygen kinetics in the Ruddlesden-Popper oxide $La_{1.85}Sr_{0.15}CuO_4$, Nat. Commun. 9 (1) (2018) 92, https://doi.org/10.1038/s41467-017-02568-z.
[41] L. Minervini, R.W. Grimes, J.A. Kilner, K.E. Sickafus, Oxygen migration in $La_2NiO_{4+\delta}$, J. Mater. Chem. 10 (2000) 2349–2354, https://doi.org/10.1039/B004212I.
[42] D. Lee, H.N. Lee, Controlling oxygen mobility in Ruddlesden–Popper oxides, Materials 10 (4) (2017) 368, https://doi.org/10.3390/ma10040368.
[43] N.L. Allan, W.C. Mackrodt, Oxygen ion migration in La_2CuO_4, Philos. Mag. A 64 (1991) 1129–1132, https://doi.org/10.1080/01418619108204884.
[44] D.J. Buttrey, P. Ganguly, J.M. Honig, C.N. Rao, R.R. Schartman, G.N. Subbanna, Oxygen excess in layered lanthanide nickelates, J. Solid State Chem. 74 (1988) 233–238, https://doi.org/10.1016/0022-4596(88)90350-7.
[45] J.-M. Bassat, M. Burriel, O. Wahaudi, R. Castaing, M. Ceretti, P. Veber, I. Weill, A. Villesuzanne, J.-C. Grenier, W. Paulus, J.A. Kilner, Anisotropic oxygen diffusion properties in $Pr_2NiO_{4+\delta}$ and $Nd_2NiO_{4+\delta}$ single crystals, J. Phys. Chem. C 117 (50) (2013) 26466–26472, https://doi.org/10.1021/jp409057k.
[46] M. Burriel, H. Tellez, R.J. Chater, R. Castaing, P. Veber, M. Zaghrioui, T. Ishikara, J.A. Kilner, J.-M. Bassat, Influence of crystal orientation and annealing on the oxygen diffusion and surface exchange of $La_2NiO_{4+\delta}$, J. Phys. Chem. C 120 (32) (2016) 17927–17938, https://doi.org/10.1021/acs.jpcc.6b05666.
[47] Y.-L. Lee, D. Lee, X.R. Wang, H.N. Lee, D. Morgan, Y. Shao-Horn, Kinetics of oxygen surface exchange on epitaxial Ruddlesden–Popper phases and correlations to first-principles descriptors, J. Phys. Chem. Lett. 7 (2) (2016) 244–249, https://doi.org/10.1021/acs.jpclett.5b02423.
[48] M.S.D. Read, M.S. Islam, F.E. Hancock, F. King, Defect chemistry of $La_2Ni_{1-x}M_xO_4$ (M= Mn, Fe, Co, Cu): relevance to catalytic behavior, J. Phys. Chem. B 103 (1999) 1558–1562, https://doi.org/10.1021/jp984059s.
[49] M.S.D. Read, M.S. Islam, G.W. Watson, F.E. Hancock, Surface structures and defect properties of pure and doped La_2NiO_4, J. Mater. Chem. 11 (10) (2001) 2597–2602, https://doi.org/10.1039/B102678J.
[50] G. Kresse, J. Hafner, Ab initio molecular dynamics for liquid metals, Phys. Rev. B 47 (1993) 558–561. https://doi:https://doi.org/10.1103/PhysRevB.47.558.
[51] G. Kresse, J. Furthmüller, Efficient iterative schemes for ab initio total-energy calculations using a plane-wave basis set, Phys. Rev. B 54 (1996) 11169–11186, https://doi.org/10.1103/PhysRevB.54.11169.
[52] A.V. Kovalevsky, V.V. Kharton, A.A. Yaremchenko, Y.V. Oivak, E.N. Naumovich, J. R. Frade, Stability and oxygen transport properties of $Pr_2NiO_{4+\delta}$ ceramics, J. Euro. Ceram. Soc. 27 (2007), 4269–4272. doi:https://doi.org/10.1016/j.jeurceramsoc.2007.02.136.
[53] E. Niwa, K. Wakai, T. Hori, K. Yashiro, J. Mizusaki, T. Nashimoto, Thermodynamic analyses of structural phase transition of $Pr_2NiO_{4+\delta}$ involving variation of oxygen content, Thermochim. Acta 575 (2014) 129–134, https://doi.org/10.1016/j.tca.2013.10.025.
[54] L. Marchetti, F. Miserque, S. Perrin, M. Pijolat, XPS study of Ni-base alloys oxide films formed in primary conditions of pressurized water reactor, Surf. Interface Anal. 47 (2015) 632–642, https://doi.org/10.1002/sia.5757.
[55] L. Tian, T. Yang, W. Pu, J. Zhang, Synthesis of cubic $Ni(OH)_2$ nanocages through coordinating etching and precipitating route for high-performance supercapacitors, Nanoscale Res. Lett. 14 (2019) 264, https://doi.org/10.1186/s11671-019-3096-6.
[56] M.T. Greiner, M.G. Helander, Z.B. Wang, W.M. Tang, Z.H. Lu, Effects of processing conditions on the work function and energy-level alignment of NiO thin films, J. Phys. Chem. C 114 (2010) 19777–19781, https://doi.org/10.1021/jp108281m.
[57] H.Q. Seo, J.W. Nam, K.D. Kim, J.K. Sim, Y.D. Kim, D.C. Lim, CO oxidation of Ni films supported by carbon fiber, J. Mol. Catal. A 361-362 (2012) 45–51, https://doi.org/10.1016/j.molcata.2012.05.001.
[58] G.D. Dwivedi, A.G. Joshi, S. Kumar, H. Chou, K.S. Yang, D.J. Jhong, W.L. Chan, A.K. Ghosh, S. Chatterjee, Electronic structure study of wide band gap magnetic semiconductor $(La_{0.6}Pr_{0.4})0.65Ca_{0.35}MnO_3$ nanocrystals in paramagnetic and ferromagnetic phases, Appl. Phys. Lett. 108 (2016) 172402–1-5, https://doi.org/10.1063/1.4947466.
[59] S.L. Stipp, M.F. Hochella Jr., Structure and bonding environments at the calcite surface as observed with X-ray photoelectron spectroscopy (XPS) and low energy

electron diffraction (LEED), Geochim. Cosmochim. Acta 55 (1991) 1723–1736, https://doi.org/10.1016/0016-7037(91)90142-R.
[60] W. Zhang, X. Li, Z. Qu, Q. Zhao, G. Chen, Facile solution synthesis and characterization of $CaCO_3$ microspheres with urchin-shaped structure, Mater. Lett. 64 (2010) 71–73, https://doi.org/10.1016/j.matlet.2019.126602.
[61] R.D. Shannon, C.T. Prewitt, Effective ionic radii in oxides and fluorides, Acta Crystallogr. Sect. B Struct. Crystallogr. Cryst. Chem. 25 (1969) 925–946. https://doi:https://doi.org/10.1107/S0567740869003220.
[62] G. Henkelman, A. Arnaldsson, H. Jónsson, A fast and robust algorithm for Bader decomposition of charge density, Comput. Mater. Sci. 36 (2006) 354–360, https://doi.org/10.1016/j.commatsci.2005.04.010.